Eur. Phys. J. Special Topics **224**, 369–378 (2015)

DOI: 10.1140/epjst/e2015-02366-2

THE EUROPEAN PHYSICAL JOURNAL SPECIAL TOPICS

Regular Article

# Instabilities of nanoscale patterned metal films

L. Kondic[1,a], N. Dong[1], Y. Wu[2], J.D. Fowlkes[3], and P.D. Rack[2,3]

[1] Department of Mathematical Sciences, New Jersey Institute of Technology, Newark, NJ 07102, USA
[2] Department of Materials Science and Engineering, The University of Tennessee, Knoxville, Tennessee 37996, USA
[3] Center for Nanophase Materials Sciences, Oak Ridge National Laboratory, Oak Ridge, Tennessee 37381, USA

Received 10 August 2014 / Received in final form 16 February 2015
Published online 8 April 2015

**Abstract.** We consider the evolution and related instabilities of thin metal films liquefied by laser pulses. The films are patterned by large-scale perturbations and we discuss how these perturbations influence the dynamics. In the experiments, we find that the considered thin films dewet, leading to the formation of primary and secondary drops, with the locations of the primary ones coinciding with the original perturbations. Based on the results of the fully nonlinear time-dependent simulations, we discuss the details of the evolution leading to these patterns. Furthermore, in both experiments and simulations, we discuss the influence of the shape of the initial perturbations on the properties of the final patterns.

## 1 Introduction

Instabilities of thin liquid films are of importance in a variety of applications. In particular, thin metal films and the patterns that form during their evolution find its relevance for plasmonic enhanced functionalities such as surface-enhanced Raman spectroscopy (SERS) [2,19,21,22] and magnetic nano-particles [14,21], among others. In addition to their applications, these films serve as systems that can be used to test the application of continuous fluid mechanics on nanoscale. One advantage of metal films over other materials is that it is possible to control very precisely their initial configuration (e.g. by lithographic techniques) and then, after the films are liquefied, follow their evolution starting from the precisely known initial condition. Such a setup allows for a direct comparison between experiments and simulations that cannot be easily achieved with other materials.

Thin metal films and their instabilities have been considered extensively in the literature, see e.g., [13,16,20,24,25,29] and references therein. In our recent works [8,9,18,26], we have started analyzing the interplay between the instability development and initial geometry of the films. While analyzing instabilities in the problems where contact lines are initially present is of significant interest, it is even

[a] e-mail: kondic@njit.edu

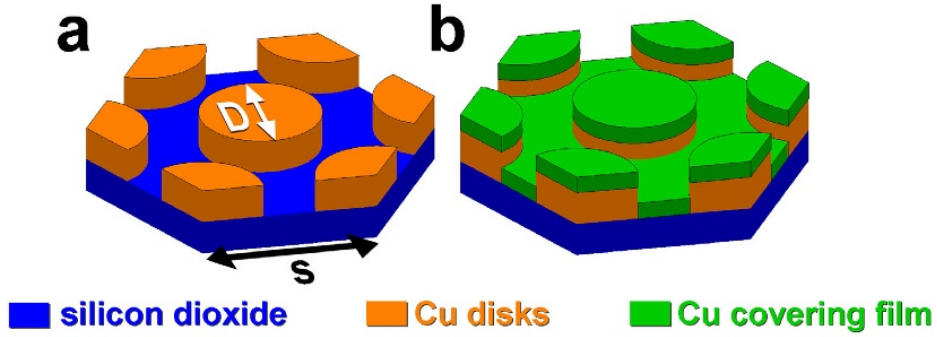


**Fig. 1.** Illustration of the patterning process. The first step involves patterning cylinder arrays of diameter $D$ and the distance $S$ (orange). The second step involves covering the cylinder with a continuous thing film (green).

more insightful, from the point of view of understanding the instability mechanisms, to consider configurations involving dewetting. In our recent work [26] we have reported experiments involving thin films patterned by disk-like perturbations. The focus of the present paper is to discuss in more detail the underlying instability mechanism in such a geometry, with the focus on the role of destabilizing liquid-solid interaction forces. Furthermore, we present new experimental and simulation results where we vary geometric properties of the imposed perturbations and discuss the influence that these properties have on the instability development.

## 2 Experiments

The details of experimental procedure can be found in [26]. Here we just briefly review the main process flow as illustrated in Fig. 1. The metal thin film geometry was realized by two steps. Initially 9 nm thick Cu cylinders, squares and triangles were patterned using electron beam (EB) lithography on a 100 nm amorphous thermal $SiO_2$ film on a Si substrate. During the lithography step, ≈200 nm thick PMMA resist was used and the patterns were exposed to 1200 $\mu$C/cm$^2$ 100 keV focused EB. After metallization using an AJA DC sputtering chamber and liftoff of the resist, the patterned copper shapes were immediately loaded to the vacuum chamber of the DC sputtering system to prevent oxidation of Cu, and a continuous 9 nm thick Cu top layer was sputtered on top of the patterned shapes and substrate. The patterned Cu film was then exposed to an 18 ns, 248 nm KrF excimer laser. Limited oxidation is expected due to the continuous experimental steps considering that the initial oxidation rate of copper is slow (≈0.031 nm/day) [4]. The pulse energy is selected to be 140 mJ/cm$^2$ to elevate thin film temperature above its melting point (1358 K) and the corresponding liquid lifetime was estimated by thermal simulations [26]. The estimated maximum temperature and liquid life time of a 9 nm film and a 20 nm film using thermal simulation are ≈1872 K (≈26 ns liquid time) and ≈2000 K (≈37 ns liquid time) respectively. We note that since the 248 nm excimer laser wavelength is far from the range of plasmonic resonance of the patterned Cu nanostructures (high energy mode located at ≈600 − 800 nm), we ignore plasmonic heating in this study. We note that the fluence range for the Cu melting is below a typical ablation threshold and rapid heating and cooling minimizes Cu evaporation and diffusion into the substrate [27].

After exposure, the liquid instability leads to spontaneous pattern formation. The novelty of the geometry considered here is the synthetic perturbations regularly

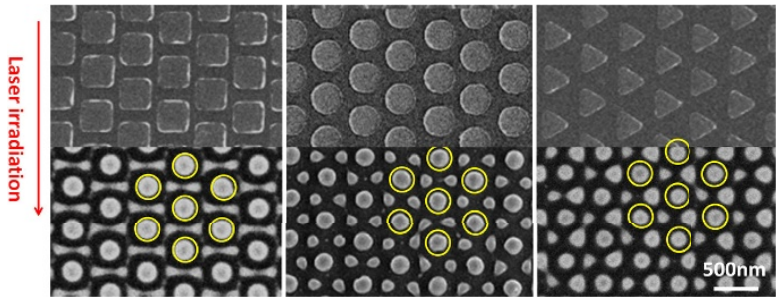


**Fig. 2.** Experimental results for the perturbations of different shapes. The top row shows the initial configurations, and the bottom row shows the resulting nanoparticles. Both the base film and the perturbations are 9 nm thick. The shapes shown have resulted after one pulse; the liquid lifetime for a single pulse is estimated as 25 ns for the 9 nm Cu film and 37 ns for the 18 nm film [26]. The transparent circles highlight the location of primary nanoparticles. The bright areas show the parts of the domain covered by the metal particles, and dark areas show the substrate. Here the distance between perturbation centers is $S = 500$ nm, and the length of a typical dimension (the edge length of squares and triangles, diameter for circles) is $D = 350$ nm.

spaced on top of the film. In [26], a variety of different thicknesses of the film and the perturbations were discussed; here we will use fixed film thickness, and consider perturbations whose aspect ratios and geometry are varied. Figure 2 shows the results for three different shapes of perturbations: disks, and four-sided and three-sided prisms. For simplicity, we will refer to these shapes as circles, squares and triangles. We see that for each considered geometry, the final pattern involves drops/particles that form at the location of the initial perturbations, with additional patterns that form in between. Clearly, the perturbation shape influences the evolution, although the final patterns that form are similar, in particular in the case of circles and triangles. Square geometry has not finished evolving during a single laser pulse, and the shape of the secondary patterns provides some insight into the dynamics. We discuss these dynamics in more detail after introducing our theoretical model.

## 3 Model

In the present work, we use an implementation of the long wave (lubrication) model for the purpose of analyzing and understanding the evolution and fluid instabilities that lead to the patterns such as the ones shown in Fig. 2. Before proceeding with more detailed description of the model, it is important to clarify one crucial point: in the experiments, after application of laser pulses, the complete domain is covered by liquid metal, and fluid fronts and corresponding contact lines are not present, at least initially. Therefore, any implemented model must include an ingredient that leads to film instability and dewetting. On nanometric length scales, as considered here, this ingredient is destabilizing liquid-solid interaction: without inclusion of this interaction, instability cannot happen. In our model, we include this interaction via so-called disjoining pressure model, discussed in some details in [7], that includes both stabilizing and destabilizing interactions. Such a model leads naturally to formation of an equilibrium film of thickness $h_*$, corresponding to the thickness at which the competing terms in the disjoining pressure balance.

After specifying the crucial component of the model, we briefly outline the main concepts. Within long wave theory, one averages over the short direction (film thickness) and ignores all gradients in the out-of-substrate-plane direction. The relevant

asymptotic expansion requires that all slopes are small: while this assumption is not satisfied at the late stages of evolution (such as the ones shown in Fig. 2) since the contact angle for Cu on $SiO_2$ is $\approx 79^\circ$ [28], it is expected to be a reasonable approximation for early stages of evolution, as soon as capillary effects smoothen the initially imposed shapes. The additional assumptions and approximations used are as follows: (i) we assume that the evolution proceeds in isothermal regime, and therefore we are ignoring transient effects at the very beginning and the very end of a laser pulse, as well as temperature dependence of material parameters, in particular of metal viscosity and surface tension. The latter may lead to Marangoni stresses; our preliminary estimates based on the thermal simulations [26] (estimates using the approximate analytical results for liquid metal temperature given in [24] lead to similar results) suggest that for the considered geometry the Marangoni effects are not dominant. (ii) phase change effects are ignored. (iii) inertial effects are also not considered in the present work; more complete model based on directly solving Navier-Stokes equations [1], as well as the experiments with Au particles [11] suggest that these effects may become important in the problem where contact lines are initially present and dewetting can proceed on a time scale faster than the evolution considered in the present work. Arguably, these approximations should be reconsidered and we are currently in the process of analyzing their influence; however, at this point, we aim to formulate a minimal model that can provide an initial insight into the considered problem. Similar approach has been used in our earlier works, see e.g., [8,10,13,27].

Following the approach outlined above, one obtains the following 4th order partial differential equation describing evolution of a liquid film of thickness $h(x, y, t)$, where $(x, y)$ are the in-plane coordinates:

$$3\mu\frac{\partial h}{\partial t} + \gamma\nabla\cdot(h^3\nabla\nabla^2 h) + \nabla\cdot[h^3\nabla\Pi(h)] = 0. \tag{1}$$

Here, $\mu$ and $\gamma$ are the fluid viscosity and surface tension, respectively, assumed to be space and time independent. The second term corresponds to capillary forces, and the third one models liquid-solid interaction; $\Pi$ is the disjoining pressure, describing the interaction of the liquid metal with the solid substrate. This interaction may be very complex and it is not well understood [27]. Following the approach of formulating a minimal model that still has a potential to provide useful insight, we consider the disjoining pressure of a simple power-law form

$$\Pi(h) = \kappa f(h) = \kappa\left[\left(\frac{h_*}{h}\right)^n - \left(\frac{h_*}{h}\right)^m\right]. \tag{2}$$

Such a form of disjoining pressure with $(n, m) = (3, 2)$ was used to describe instabilities of thin (unstructured) metal films [10]. Here, $\kappa = s/(Mh_*)$, where $M = (n-m)/((n-1)(m-1))$, and $s = \gamma(1-\cos\theta)$, where $\theta$ is the contact angle. The Hamaker constant, $A$, is related to $\kappa$ by $A = 6\kappa h_*^3$ [7].

To proceed, we analyze this evolution equation coupled with no-flux, zero-derivative boundary conditions: $h_{xxx} = h_{yyy} = h_x = h_y = 0$. This choice preserves mass in the computational domain, furthermore, the use of zero-derivative boundary condition allows (for circular and square geometries) an implementation of boundaries as symmetry lines. This feature is useful since in simulations we consider only a subset of the experimental domains shown in Fig. 2. For triangular geometries, we use periodic boundary conditions[1].

[1] The authors acknowledge help by Te-Sheng Lin with implementation of periodic boundary conditions.

Before proceeding with the analysis of Eq. (1), we write it down in non-dimensional form. For this purpose, we introduce the viscous time scale, $t_c = 3\mu h_c/\gamma$, where $h_c = 1$ nm is the chosen length scale. Then, we define non-dimensional variables (with bars) by $h = \bar{h}h_c$, $t = \bar{t}t_c$, $x = \bar{x}h_c$, $y = \bar{y}h_c$. After the non-dimensionalization, we obtain (for simplicity we drop all the bars)

$$\frac{\partial h}{\partial t} + \nabla \cdot (h^3 \nabla \nabla^2 h) + K \nabla \cdot [h^3 f'(h) \nabla h] = 0. \tag{3}$$

Here, $K = \kappa h_c/\gamma$. For the material parameters corresponding to Cu on $SiO_2$ substrate, given in [28], we find $t_c = 1.008 \times 10^{-11}$ s, and $K = 1.608$.

## 4 Results

In this section, we start by discussing the results of the linear stability analysis (LSA) of Eq. (3) and then continue with describing the outcomes of fully nonlinear time dependent simulations. The LSA is expected to provide the basic understanding of the instability mechanism, since it is carried out assuming that the base state is a flat film, and furthermore, by design it applies only to the early stages of evolution. However, as we will see in what follows, this approach does provide useful insight in particular regarding evolution of the flat film in between the perturbations.

### 4.1 Linear Stability Analysis

The LSA is carried out by considering initially flat film of thickness $h_0$, and assuming that this flat film is perturbed by small perturbations: $h(x,t) = h_0 + \delta \exp(iqx + \sigma t)$, where $\delta \ll 1$, $q = 2\pi/\lambda$ is the wavenumber and $\sigma$ is the growth rate. Assuming this form of $h$ in Eq. (3), and collecting the terms linear in $\delta$, we obtain the following dispersion relation

$$\sigma = -h_0^3 q^4 - K h_0^3 f'(h_0) q^2. \tag{4}$$

As expected, the perturbations characterized by large $q$'s (short wavelengths) are stabilized by surface tension, and the growth rate for small $q$'s converges to zero as $q \to 0$. The wavelength of maximum growth, $\lambda_m$, corresponding to the largest growth rate, $\sigma_m$, is considered to be the most "dangerous", meaning that one expects (at least within the linear picture) that the instabilities characterized by wavelengths close to $\lambda_m$ show up in physical experiments. Both $\lambda_m$ and $\sigma_m$ depend on $h_0$; to gain basic understanding, take $h_0 = 13.5$ (average of the base film thickness and the total thickness of the perturbations, ignoring the equilibrium film thickness). We then find that $h_c\lambda_m \approx 260$ nm, and the time for which instability is expected to grow, $t_c/\sigma_m \approx 11.95$ ns. Recalling the experimental time scale on which instabilities develop ($\approx 20 - 30$ ns), we see that the predictions of the LSA are consistent with the experimental data; furthermore, the LSA suggests that the in-plane dimensions of the film in between the perturbations are comparable to $h_c\lambda_m$, and therefore it is reasonable to expect thin-instability to be relevant in the experiments considered. The various mechanisms that may lead to instability of thin films have been extensively discussed in the literature, particularly in the context of polymeric [3,23], liquid crystal [12] and metal films [10,13,25], see [5,17] for reviews. For the present purposes, we only note that this instability may be driven either by experimental noise of various (thermal, mechanical) origins, or also, in the present context, by the fact that large imposed perturbations may induce dynamics that will lead to instability of the film in between the perturbations. We discuss these dynamics next in the context of the results of numerical simulations.

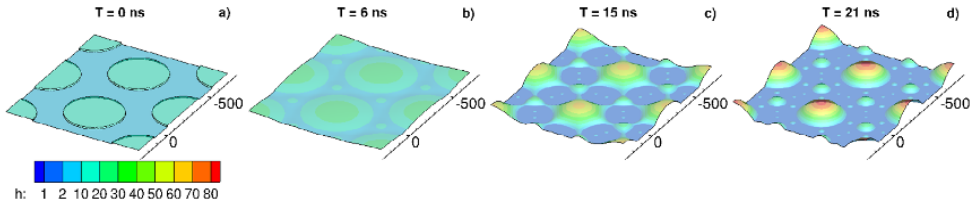


**Fig. 3.** Evolution of a flat film of the thickness of 10 nm, with imposed 9 nm thick disk-like perturbations. The diameter of the disks is $D = 350$ nm, and the distance between disk centers is $S = 500$ nm, as in Fig. 2.

### 4.2 Nonlinear simulations: Reference case

Here we proceed by discussing the results of the simulations of the evolution Eq. (3). These simulations are based on ADI-type of scheme that allows for efficient computation of two dimensional problems considered here [15].

Figure 3 shows an example of the evolution where the initial perturbation, shown in part (a) is of circular shape. The whole domain is covered by a 10 nm thick film (so, 9 nm above the equilibrium film thickness) and on top of this film we add 9 nm thick cylinders. This geometry closely resembles the one used in the experiments, shown in Fig. 2, second column. To avoid infinite gradients of the initial profile we smoothen the perturbation boundaries in a narrow transition region; the size of this transition region does not influence the results that follow, as long as its size is much smaller than the cylinder diameter, $D$.

Figure 3 shows that, as soon as the evolution starts, the surface tension effects lead to formation of large drops on top of the film. In between these large drops, in the particular case shown in the figure, smaller, secondary drops form, see part (b). These secondary drops are essentially due to the fluid being pushed away during spreading of the initial perturbations, and form exactly in between any three original perturbations. A detailed inspection of the results show that, while the film is thicker at the location of the secondary drops, it is slightly thinner at the points that are furthest away from the secondary drops (due to the imposed symmetry, these points are at the intersection between the lines connecting the centers of the secondary drops and the lines connecting the centers of the primary drops. These locations are the most unstable due to the presence of van der Waals forces, and here is where the film dewets (the thickness reaches $h_*$), see part (c). In the particular case shown in Fig. 3, the further evolution involves formation of filaments between the primary and secondary drops. As the dynamics proceeds, these filaments break up by the process resembling Rayleigh-Taylor instability of a liquid jet (see, e.g., [6] for extensive discussion of this problem). These breakups lead to the formation of tertiary drops that are smaller in size than the secondary ones. The final result is the network of drops or different sizes, see part (d). By comparing with the LSA, we note that, as expected, the instability develops on the consistent time scale. A comparison with the experimental results, see Fig. 2, second column, shows that secondary drops develop at consistent locations between the simulations and experiments. A careful examination of the experimental result after application of laser pulses uncovers also smaller, tertiary drops in some cases. The simulation results suggest that these drops may be due to the breakup of filaments that form in between the primary and secondary drops. Therefore, we find that, at least for the considered case, our simulations, although based on a rather simple model, compare favorably with the experiments.

After outlining the basic picture of instability development, we proceed in Sect. 4.3 to discuss the influence of the shape of the imposed perturbations on the final pattern. Before that, we note in passing some additional features of the instability

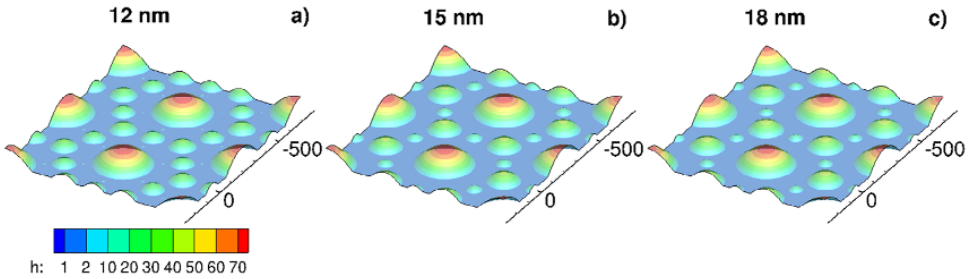


**Fig. 4.** Final shapes obtained from the disk-like perturbations whose aspect ratio is varied: the volume of the perturbations is the same as in Fig. 3. The perturbations' thickness is shown for the each snapshot. See Fig. 3 for the final shape for 9 nm thick perturbations.

development, observed both in experiments and simulations [26]. First, placing the perturbations very close together, while keeping their size fixed, may lead (in simulations) to full merge of the perturbations and the final result may just be a film of uniform thickness determined by the mass conservation. In experiments (or in simulations with superimposed perturbations, as discussed further below), such a film breaks up, again due to destabilizing liquid-solid interaction, leading however to irregularly spaced drops. On the other hand, if the initial perturbations are placed far apart, the metal film in between has sufficient time to become unstable and this instability leads to the formation of disordered drops in between the main ones that form at the locations of the original perturbations. This effect was also observed in the simulations where the initial condition was perturbed by a set of random perturbations [26]. In between these two extremes, there is a regime where a regular array of drops forms, both in the experiments, see Fig. 1a and in the simulations, see Fig. 3. We focus on this regime in what follows.

### 4.3 Nonlinear simulations: Shape dependence

We proceed by discussing the influence of the shape of the imposed perturbations on the dynamics. Here are some questions that we will consider: (i) Assuming that the considered perturbation is of disk-like shape, what is the influence of the aspect ratio of the perturbation on the evolution? (ii) What is the influence of perturbation shape on the evolution? For example, if we have perturbations with the base of triangular or square shape, how is the evolution influenced?

Figure 4 shows the final outcomes of the simulations where the aspect ratio of the disk-like perturbations was varied – we consider perturbations that are thicker, but their volume is kept fixed. While the generic features of the results are similar for all aspect ratios, some differences can be seen as well. One of the differences is the size of the primary drops, which decreases as the perturbation thickness increases. This could be explained by realizing that thicker perturbations collect less of the material from the underlying film during their evolution since their diameter is smaller. Therefore, by varying the aspect ratio of the perturbations, one can control the size of the primary particles. The second difference is the distribution and size of the secondary and tertiary drops. While some features of the final results depend on the details of the dynamics, the main difference between the results shown in Fig. 4 and Fig. 3d) is that for the cases shown in Fig. 4, the filaments do not form between the primary and secondary drops (these filaments lead to tertiary drops visible in Fig. 3d), since the primary drops are smaller in size here. Instead, filaments form between the secondary drops themselves, and their breakup then leads to the formation of tertiary drops that

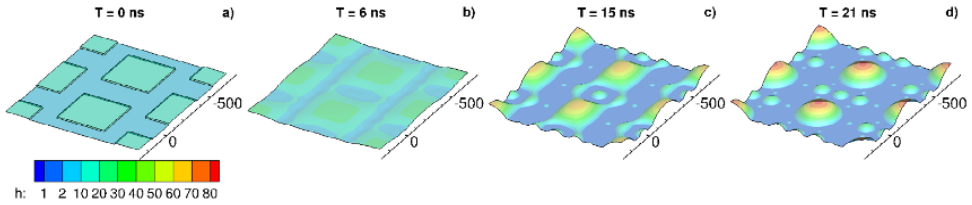


**Fig. 5.** Evolution of square-like perturbations. The distance between the squares' centers is 500 nm, and the length of a square edge is 350 nm, as in Fig. 2.

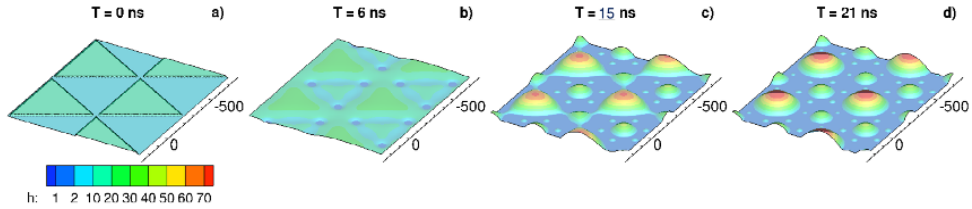


**Fig. 6.** Evolution of triangle-like perturbations. The distance between the triangles' centers is 500 nm, and the length of a triangle edge is 350 nm, as in Fig. 2.

differ in size, depending on the size of the secondary drops. We note that simulations turn out to be very useful in understanding the details of the dynamics since they provide detailed insight into the evolution, that cannot be reached by considering experimental results alone.

Figures 5 and 6 show the results of simulations where the perturbations are the prisms with either square or triangular base, respectively. The perturbations are arranged in the same manner and are of the same size as the experimental ones shown in Fig. 2. We observe that the symmetry of the distributions of perturbations plays an important role. For triangular perturbations, distributed in a symmetric fashion, the final outcome is similar to the one observed for circular perturbations, compare Fig. 6d and Fig. 3d, although the intermediate stages of evolution may be very different, compare, e.g., Fig. 6b and Fig. 3b. In the particular case of triangles considered here, we note that the secondary drops form by two separate mechanisms - either by instability of the film in between the perturbations (mechanism I, similarly as for the circles), or by separation of some of the material that was originally a part of the main drops (mechanism II). Careful examination of the results shown in Fig. 6b shows that the drops produced by the mechanism I are slightly larger. This difference is more pronounced in the experiments, see Fig. 1, right column; this difference may be a consequence of simplified modeling assumptions used in the present work.

If the distribution and shape of the perturbations are not symmetric, as in the case of square-like perturbations shown in Fig. 5, then both the evolution and the final outcome are different; small differences in the early stages of evolution lead to formation of the filaments between some of the original perturbations, and the breakups of these filaments then lead to non-symmetric distribution of the secondary particles. The experimental results, shown in Fig. 2, are consistent with the simulations: note much higher degree of symmetry (and similarity) for triangular and circular perturbations versus square ones.

Here we have considered the evolution of different perturbation shapes for a particular perturbation size and distance; of course, changing these parameters will in general lead to different results. However, we find that in all cases that we have analyzed, very useful insight can be reached by considering basic mechanisms leading to

instability, in particular thin film and filament breakups that were considered in the earlier works [6,7].

## 5 Conclusions

In the present work, we have focused on the influence of controlled large-scale perturbations of a flat film on its evolution. We show, both experimentally and computationally, that these perturbations can be used to control and direct this evolution, leading as a result to formation of ordered arrays of drops/particles. Furthermore, we show that the geometric properties of these arrays depend on the degree of symmetry satisfied by the distribution and shape of the original perturbations.

Another important finding is that continuum fluid mechanics, and its long wave limit, augmented by inclusion of liquid-solid interaction in the model, prove to be extremely useful in developing better insight into the dynamics and development of instabilities on nanoscale.

For the considered problem of metal films irradiated by laser pulses, there is much more to be done, including consideration of thermal effects and resulting Marangoni stresses, inclusion of phase change, inertial effects, and development of models appropriate for large contact angles. Our work in these directions continues.

L. Kondic and N. Dong acknowledge support by NSF grant No. CBET-1235710. Y. Wu acknowledges support from the TN-SCORE program funded by NSF EPS 1004083. J.D. Fowlkes acknowledges that the portion of this work related to the deposition of thin films and nanolithography was conducted at the Center for Nanophase Materials Sciences, which is sponsored at Oak Ridge National Laboratory by the Scientific User Facilities Division, Office of Basic Energy Sciences, U.S. Department of Energy. P.D. Rack acknowledges support from NSF grant No. CBET- 1235651.

## References

1. S. Afkhami, L. Kondic, Phys. Rev. Lett. **111**, 034501 (2013)
2. H.A. Atwater, A. Polman, Nature Materials **9**, 9 (2010)
3. J. Becker, G. Grün, R. Seemann, H. Mantz, K. Jacobs, K.R. Mecke, R. Blossey, Nature Mat. **2**, 59 (2003)
4. G.H. Chan, J. Zhao, E.M. Hicks, G.C. Schatz, R.P. Van Duyne, Nano Letters **7**, 1947 (2007)
5. R.V. Craster, O.K. Matar, Rev. Mod. Phys. **81**, 1131 (2009)
6. J. Diez, A. Gonzalez, L. Kondic, Phys. Fluids **21**, 082105 (2009)
7. J. Diez, L. Kondic, Phys. Fluids **19**, 072107 (2007)
8. J.D. Fowlkes, L. Kondic, J. Diez, P.D. Rack, Nano Letters **11**, 2478 (2011)
9. J.D. Fowlkes, L. Kondic, J. Diez, A.G. González, J. Wu, N. Roberts, C. McCold, P.D. Rack, Nanoscale **4**, 7376 (2012)
10. A.G. Gonzalez, J.D. Diez, Y. Wu, J.D. Fowlkes, P.D. Rack, L. Kondic, Langmuir **13**, 9378 (2013)
11. A. Habenicht, M. Olapinski, F. Burmeister, P. Leiderer, J. Boneberg, Science **309**, 2043 (2005)
12. S. Herminghaus, K. Jacobs, K. Mecke, J. Bischof, A. Fery, M. Ibn-Elhaj, S. Schlagowski, Science **282**, 916 (1998)
13. L. Kondic, J. Diez, P. Rack, Y. Guan, J. Fowlkes, Phys. Rev. E **79**, 026302 (2009)
14. H. Krishna, A.K. Gangopadhyay, J. Strader, R. Kalyanaraman, J. Magn. Magn. Mater **323**, 356 (2011)

15. T.-S. Lin, L. Kondic, A. Filippov, Phys. Fluids **24**, 022105 (2012)
16. Y.-J. Oh, J.-H. Kim, C.V. Thompson, C.A. Ross, Nanoscale **5**, 401 (2013)
17. A. Oron, S.H. Davis, S.G. Bankoff, Rev. Mod. Phys. **69**, 931 (1997)
18. N.A. Roberts, J.D. Fowlkes, K. Mahady, S. Afkhami, L. Kondic, P.D. Rack, ACS Appl. Mat. Interfaces **5**, 4450 (2013)
19. C.E. Rodrguez, R.J. Pelez, C.N. Afonso, S. Riedel, P. Leiderer, D. Jimenez-Rey, A. Climent-Font, Appl. Surf. Sci. **302**, 32 (2014)
20. F. Ruffino, A. Pugliara, E. Carria, L. Romano, C. Bongiorno, C. Spinella, M.G. Grimaldi, Nanotechnology, 23 (2012)
21. R. Sachan, V. Ramos, A. Malasi, S. Yadavali, B. Bartley, H. Garcia, G. Duscher, R. Kalyanaraman, Adv. Mat. **25**, 2045 (2013)
22. S. Sarita, E.S. Ozen, A. Aydinli, J. Optoelectronics Adv. Mat. **15**, 10 (2013)
23. R. Seemann, S. Herminghaus, K. Jacobs, Phys. Rev. Lett. **86**, 5534 (2001)
24. J. Trice, D. Thomas, C. Favazza, R. Sureshkumar, R. Kalyanaraman, Phys. Rev. B **75**, 235439 (2007)
25. J. Trice, D. Thomas, C. Favazza, R. Sureshkumar, R. Kalyanaraman, Phys. Rev. Lett. **101**, 017802 (2008)
26. Y. Wu, N. Dong, S. Fu, J.D. Fowlkes, L. Kondic, M.A. Vincenti, D. de Ceglia, P.D. Rack, ACS Appl. Mater. Interfaces **6**, 5835 (2014)
27. Y. Wu, J.D. Fowlkes, P.D. Rack, J.A. Diez, L. Kondic, Langmuir **26**, 11972 (2010)
28. Y. Wu, J.D. Fowlkes, N.A. Roberts, J.A. Diez, L. Kondic, A.G. González, P.D. Rack, Langmuir **27**, 13314 (2011)
29. S. Yadavali, M. Khenner, R. Kalynaraman, J. Mat. Res. **28**, 1715 (2013)